Nano Energy 66 (2019) 104134

Contents lists available at ScienceDirect

Nano Energy

journal homepage: http://www.elsevier.com/locate/nanoen

Full paper

$Ti_3C_2T_x$ MXene-graphene composite films for wearable strain sensors featured with high sensitivity and large range of linear response

Yina Yang [a,b,c], Zherui Cao [a,b], Peng He [d], Liangjing Shi [a], Guqiao Ding [d], Ranran Wang [a,*], Jing Sun [a]

[a] State Key Laboratory of High Performance Ceramics and Superfine Microstructure Shanghai Institute of Ceramics Chinese Academy of Science, Shanghai, 200050, China
[b] University of Chinese Academy of Sciences, Beijing, 100049, China
[c] State key Laboratory of Robotics, Shenyang Institute of Automation, Chinese Academy of Science, 110016, China
[d] State Key Laboratory of Functional Materials for Informatics, CAS Center for Excellence in Superconducting Electronics (CENSE), Shanghai Institute of Microsystem and Information Technology, Chinese Academy of Sciences, Shanghai, 200050, China

ARTICLE INFO

Keywords:
Strain sensors
Layered structure
$Ti_3C_2T_x$
Multilayer graphene
Linear response

ABSTRACT

Strain sensors featured with high sensitivities and large ranges of linear responses are currently under urgent needs. Herein, we present a spontaneously formed $Ti_3C_2T_x$/graphene/PDMS layered structure, which can be divided into two layers when being stretched: a $Ti_3C_2T_x$ dominated brittle upper layer and a flexible graphene/PDMS composite bottom layer. The balance between the destruction and maintenance of the conductive pathways through the synergetic motion of the upper and bottom layers ensure a high and steady gauge factor of the senor in a wide strain range (e.g., gauge factors of 190.8 and 1148.2 in strain ranges of 0–52.6% and 52.6–74.1%, respectively). The $Ti_3C_2T_x$/graphene/PDMS layered structure based strain sensor is also featured with a low detection limit (~0.025%), a high linearity ($R^2 > 0.98$), a high cycling stability (over 5000 cycles), and an accurate monitoring of full-range human motions. Different breathing patterns in yoga are distinguished to demonstrate the practicability of the sensor.

1. Introduction

Demands for flexible and wearable electronic sensors have increased dramatically as people's desires for real-time health monitoring and human motion detection have gradually increased in recent years [1–3]. In general, to evaluate the sensing performance of a strain sensor, the sensitivity (i.e., gauge factor (GF)) and working range are regarded as the two most critical performance indicators, which unfortunately are mutually constrained [4–9] since the high sensitivity requires large changes in electrical resistance of the sensor under slight strains, while with regards to the wide working range, the sensor is required to maintain good conductive pathways during the whole stretching process. To meet the requirements of monitoring the full-range body motions of humans, the sensing ranges of strain sensors are usually required to be larger than 50%, with the sensitivity higher than 100 over the entire strain sensing range [4]. In addition, compared with the high sensitivity obtained at large strains, it is more desirable to achieve a high and stable sensitivity with linear responses within a wide strain range [1].

In order to fabricate a strain sensor with a high comprehensive sensing performance, a common strategy is to fabricate strain sensors with special architectures based on complicated processes such as pre-stretching [10,11], and 3D printing [12,13]. Given the high requirements for the rationality of structural designs and the fineness of craftsmanship, innovation of sensing materials may be a more efficient way. Currently used sensing materials mainly include carbon materials (e.g. carbon black, carbon nanotubes and graphene) [14–21], metal materials (e.g. Ag nanowires and Au nanoplates) and so on [22–29]. However, a sensing material with an unitary morphology is generally subject to its own structural characteristics and cannot simultaneously take both sensitivity and stretchability into account. For example, zero-dimensional materials normally suffer from low sensitivities and narrow sensing ranges because of their small aspect ratios [23,27]. For example, Park et al. fabricated a strain sensor based on a Au nanoparticle thin film, and the sensor exhibited a maximum GF of 2.05 at the maximum strain of 20% [27]. One-dimensional materials are inclined to

---

* Corresponding author.
E-mail address: wangranran@mail.sic.ac.cn (R. Wang).

https://doi.org/10.1016/j.nanoen.2019.104134
Received 17 July 2019; Received in revised form 4 September 2019; Accepted 24 September 2019

exhibit substantial stretchabilities and endow the strain sensor with a wide strain sensing range [21,22,28,29]. Cheng et al. presented an Au nanowires based strain sensor, which can be stretched as wide as 350% [28], and the enokitake-like Au nanowire based strain sensor made by the same team demonstrated a ultrahigh stretchability of 800% strain. [29]. While two-dimensional materials are more easily to demonstrate extremely high sensitivities in very small strain ranges but poor linearities, which can be attributed to the non-effective slippage of the adjacent stacked sheets For instance, Zhu et al. presented a graphene woven fabrics based strain sensor, which showed a ultrahigh GF of 10^6 under a small strain below 10% and the relative resistance varied almost exponentially with strain [30]. Therefore, it may be an effective consideration to compound multiple materials with various microstructures together to realize efficient synergistic motions, meeting the requirements of capturing and monitoring the full-range human motion signals [31,32].

MXenes represent a new class of two-dimensional early transition metal carbide or carbonitride (e.g., $Ti_3C_2T_x$, Ti_2CT_x, Ti_3CNT_x (T stands for the terminal groups of MXenes, x denotes the number of T) with high metallic conductivity, good oxidation resistance and excellent mechanical properties [33–36], which have set off a research boom in energy storage [37–41], electromagnetic shielding [42,43], catalytic fields [44,45], and strain sensing [46–51]. However, although MXenes are considered as two-dimensional materials, in the process of typical chemical etching, due to the destructive effect of the strong etchant (hydrofluoric acid) on the structure of MXenes, there are many irregular particles generated while the materials being delaminated into two-dimensional sheets [47]. When used as sensing materials of strain sensors, those MXene particles are prone to losing connections during the tensile processes, resulting in narrow working ranges. Thus, the introduction of rational materials to maintain the connections among MXene particles is a feasible route to simultaneously maintain high sensitivities and stretchabilities of the sensors.

In addition to the composition, the distribution of the components in the composite conductive film also has a large effect on the properties. It is generally believed that a uniform distribution of the component in the composite is more prone to achieve high sensing performances. However, a gradient distribution of the component in the composite has proven to be an effective way to simultaneously increase the sensitivity and the sensing range. Coleman et al. reported a graphene-rubber composite in which graphene had a compositional gradient change with depth. The strain sensor based on this composite exhibited an excellent comprehensive performance with a GF of 35 and a strain sensing range of 800%, surpassing most graphene based strain sensors [16].

Herein, we constructed a spontaneously formed $Ti_3C_2T_x$/graphene/PDMS layered structure, which is featured with positive and negative correlations of $Ti_3C_2T_x$ and graphene contents with the film depth, as well as the increased stacking density with the depth. The $Ti_3C_2T_x$/graphene/PDMS layered structure can be divided into two layers during the stretching process. The brittle upper layer is mainly composed of tightly stacked irregular $Ti_3C_2T_x$ particles and some multilayer graphene sheets, where cracks generate and propagate during the stretching process to dissipate tensile stresses, contributing to a high GF over 100 within the entire working range. Multilayer graphene sheets embedded in PDMS substrate constitute the flexible bottom layer and maintain the conductive pathways within a large strain range. Meanwhile, the interconnection of $Ti_3C_2T_x$ and graphene forms a nice transition layer, which ensures the integrity and durability of the whole device. The strain sensor based on $Ti_3C_2T_x$/graphene/PDMS layered structure demonstrates outstanding sensing performances, including a high sensitivity and a large linearity (GF of 190.8 within 0–52.6% and 1148.2 within 52.6–74.1%), a wide sensing range of 74.1% (~9 times larger than pure $Ti_3C_2T_x$ based strain sensors), and a low limit of detection (~0.025%) as well as high cycling stability (over 5000 cycles). Moreover, benefiting from the very simple yet efficient architecture, the $Ti_3C_2T_x$/graphene/PDMS based strain sensor requires no complicated manufacturing process, which would greatly facilitate its wide applications in practice.

2. Material and methods

2.1. Materials

Ti_3AlC_2 was purchased from Forsman Co., China. The graphite foil was purchased from Alfa Aesar Co., Inc. Hydrofluoric acid (AR, 40 wt%) and dimethylsulfoxide (AR) were purchased from China National Medicines Corporation Ltd. Terephthalic acid (PTA, AR) and NaOH (AR) were purchased from Aladdin (Shanghai, China). PDMS was purchased from Dow Corning. All chemicals were used as received without further purification. The water used throughout all experiments was purified using the Millipore system. The filter membrane was made of mixed cellulose ester, and was purchased from Merck Millipore (0.22 μm GSWP).

2.2. The synthesis of $Ti_3C_2T_x$

The synthetic method of $Ti_3C_2T_x$ was reported in a previous work. In detail, 3 g parent phase material Ti_3AlC_2 powder was slowly immersed into 30 ml 40 wt% aqueous hydrofluoric acid solution, followed by about 10 min' standing to wait for the bubbles generated by the violent reaction to disappear and the mixture to cool down. Then the mixture was reacted under continuous magnetic stirring for 6 h at room temperature and was washed with distilled water under centrifugation for several times until the pH value reached about 6. The sediment was dried by freeze drying to obtain the multilayer $Ti_3C_2T_x$ powder. 1 g as-prepared multilayer $Ti_3C_2T_x$ was added into 12 ml dimethylsulfoxide (DMSO) and stirred for 18 h, with then DMSO was removed by washing and centrifugation. The DMSO treated sediment was dispersed in 300 ml distilled water and sonicated in the iced bath under Ar atmosphere for 3 h. After being centrifuged at 3500 rpm for 1 h, the delaminated $Ti_3C_2T_x$ was obtained by collecting the upper suspension of the centrifugal product. The concentration of the suspension can be determined by ultraviolet–visible spectrum.

2.3. The synthesis of graphene

Graphene sheets used in this work were fabricated from an electrochemical method we reported before [52]. Specifically, a rectangular graphite foil (1.0 × 2.0 × 0.5 cm) based anode and a platinum foil (1.0 × 2.0 × 0.1 cm) based counter electrode were placed parallel with a spacing of 2.0 cm in the electrolyte containing 0.83 g PTA, 0.80 g NaOH and 100 ml water. Then, a constant voltage (10.0 V) was applied until the anode was exhausted within 6–8 h. The stripped products in the electrolyte were purified with water, and dried at 50 °C in an oven to obtain the powdery graphene.

2.4. The preparation of the $Ti_3C_2T_x$/Graphene film

The as-resulted graphene was mixed with $Ti_3C_2T_x$ suspension with the content of 0 wt%, 10 wt%, 25 wt%, 50 wt% and 67 wt%. Then the mixture was filtered and dried under vacuum to obtain a $Ti_3C_2T_x$/graphene conductive film.

2.5. The fabrication of the strain sensors

The PDMS monomer and curing agent were mixed with a mass ratio of 10:1, magnetically stirred for about 15 min, and then the mixture was placed in a vacuum oven for 10 min to remove bubbles. After that the PDMS was poured into a cuboid mold with the sizes of $80.0 \times 15.0 \times 1.0\ mm^3$, and was prepolymerized at 80 °C for 10 min. The $Ti_3C_2T_x$/graphene film was cut into strips with the sizes of

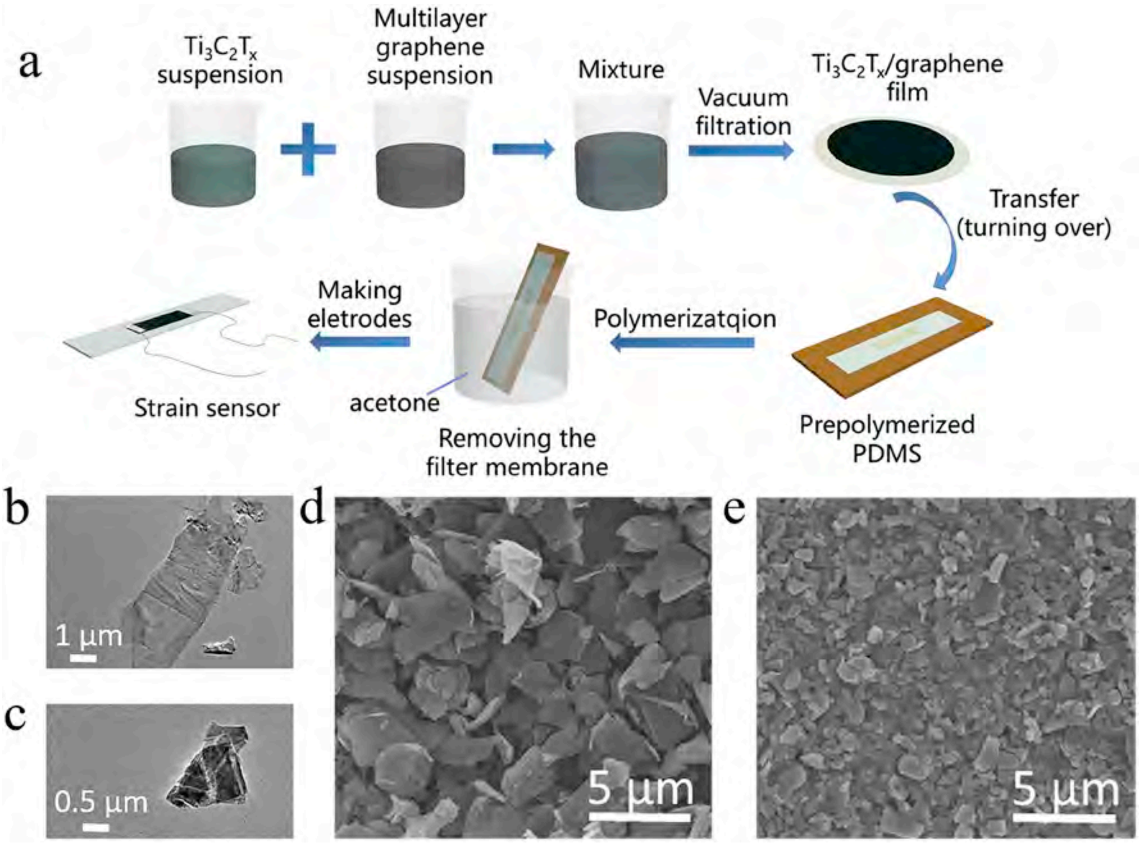

Fig. 1. a) Schematic diagram of the fabrication of the $Ti_3C_2T_x$/graphene strain sensor; transmission electron microscope (TEM) images of b) multilayer graphene and c) $Ti_3C_2T_x$; Top-view SEM images of the d) multilayer graphene and e) $Ti_3C_2T_x$ film.

$20.0 \times 6.0\,mm^2$, and was transferred onto the prepolymerized PDMS with the filter membrane facing up, followed by a polymerization progress for 1 h at 80 °C. The filter membrane was then dissolved by acetone and washed by ethyl alcohol. Finally, the silver electrodes were fixed on two sides of conductive stripes, forming a strain sensor.

2.6. *Characterization*

A high-resolution multi-function X-ray diffractometer (D8 Discover Davinci, German) was used to analyze the phase compositions and crystalline structures of samples. The morphologies of samples were characterized by a field emission scanning electron microscope (S-4800, Hitachi, Japan), a transmission electron microscope (JEM-2100F, JEOL, Japan) and an atomic force microscope (NTEGRA, NT-MDT, Russia). The concentration of the $Ti_3C_2T_x$ suspension was calibrated by an ultraviolet–visible spectrophotometer (PerkinElmer Lambda 950, USA). A high-precise electronic universal testing machine (CMT6103, MTS Systems, China) was used to test the sensing performance of strain sensors where the current signal was collected by an electrochemical workstation (PARSTAT 2273, Princeton Applied Research).

3. Morphology and structure analysis

The fabrication process of the $Ti_3C_2T_x$/graphene/PDMS layered structure based strain sensor is schematically illustrated in Fig. 1a. Shortly, a $Ti_3C_2T_x$ suspension prepared by a chemical liquid etching method and a multilayer graphene suspension prepared by an electrochemical exfoliation method were mixed with various ratios and filtrated into a conductive film with a consistent thickness of 1.4 μm (Fig. A1). Then the $Ti_3C_2T_x$/graphene films were transferred to prepolymerized polydimethylsiloxane (PDMS) substrates to form flexible and stretchable strain sensors. It must be noted that the composite film was turned over during the transferring process, with the filter membrane facing up. After post-polymerization, the filter membrane was dissolved in acetone, and the strain sensor was finally obtained by fabricating electrodes and connecting conducting wires. Fig. 1b–c show the morphology of multilayer graphene and $Ti_3C_2T_x$. It is observed that the graphene is multilayered with the lateral size of 1–6 μm (Fig. 1b) and the thickness is about 4–15 nm (Fig. A2a and Fig. A3), while $Ti_3C_2T_x$ is mainly made up of irregular particles with the size of 1–2 μm (Fig. 1c). In addition to irregular particles, some thin sheets with the thickness of 2–3 nm and the lateral size of 200–300 nm were also located within $Ti_3C_2T_x$ (Fig. A2b), which were peeled off from the accordion like $Ti_3C_2T_x$ bulks (Fig. A4) during the delamination process. The differences in the morphologies of multilayer graphene and $Ti_3C_2T_x$ can be more intuitively distinguished by the scanning electron microscope (SEM) images of graphene powders and $Ti_3C_2T_x$ thin films (Fig. 1d–e).

The multilayer graphene suspension with diverse concentrations was uniformly mixed with the $Ti_3C_2T_x$ suspension, and a series of $Ti_3C_2T_x$/graphene composite films were fabricated by the vacuum filtration method. For simplicity, the composite films were named as "$Ti_3C_2T_x/G_y$" according to the content of graphene (G means multilayer graphene, and y represents the content of graphene). Fig. A5a shows the X-ray diffraction (XRD) patterns of $Ti_3C_2T_x$, graphene and $Ti_3C_2T_x$/graphene composite with the mass ratio of 1:1. The characteristic peaks of pure $Ti_3C_2T_x$ and graphene were at around 7° and 26°, respectively. There is no doubt that the XRD pattern of $Ti_3C_2T_x$/graphene composite integrates the characteristics of pure $Ti_3C_2T_x$ and graphene, proving a nice combination of these two materials. The Raman spectra of $Ti_3C_2T_x$, graphene and $Ti_3C_2T_x$/graphene composite indicates a similar result in comparison with the XRD pattern (Fig. A5b). To further disclose the combined state of $Ti_3C_2T_x$/graphene composites, SEM images of $Ti_3C_2T_x$/graphene composites with various mass ratios are presented in Fig. 2a-d. With regard to $Ti_3C_2T_x/G_{0.1}$, it is observed that $Ti_3C_2T_x$ particles are the

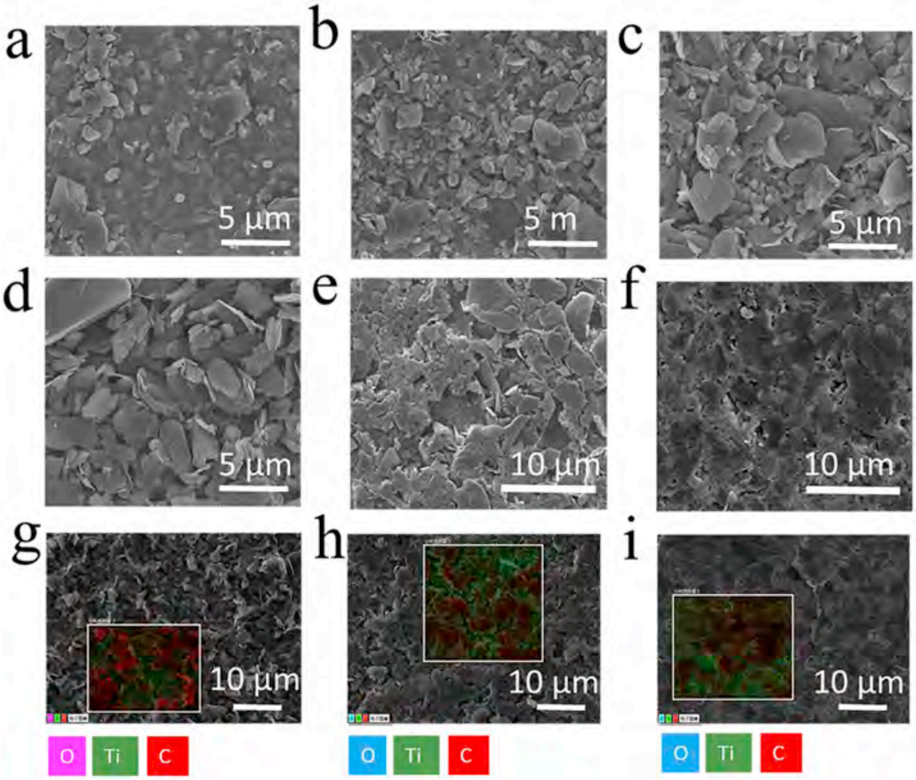

Fig. 2. Top-view SEM images of a) $Ti_3C_2T_x/G_{0.1}$, b) $Ti_3C_2T_x/G_{0.25}$, c) $Ti_3C_2T_x/G_{0.5}$, d) $Ti_3C_2T_x/G_{0.67}$. Top-view SEM images of the $Ti_3C_2T_x/G_{0.5}$ film that was scraped off e) one layer and f) two layers by tape. g) Element mapping of the intact $Ti_3C_2T_x/G_{0.5}$ film. Element mapping of the $Ti_3C_2T_x/G_{0.5}$ film that was scraped off h) one layer and i) two layers by tape.

majority components, accompanied with a small amount of graphene thick sheets (Fig. 2c). As the content of graphene increases, a lot of large graphene sheets are loosely deposited on the surface of the film (Fig. 2d–e). When the graphene content reaches 67%, the graphene sheets almost cover the entire surface of the film, and if the graphene content is further increased, the composite film can not be formed due to the powder nature of multilayer graphene.

Fig. 2e and Fig. 2f demonstrate the SEM images of the $Ti_3C_2T_x/G_{0.5}$ film that was scraped off one layer and two layers by tape, respectively. Compared with the intact film in Fig. 2c, it is obvious that the stacking density of the $Ti_3C_2T_x$/graphene composite film increased vertically through the film, and large-sized multilayer graphene sheets gradually reduced while small-sized irregular $Ti_3C_2T_x$ particles increased in number and packed closely. In order to further confirm the changes in the composition of the composite film with the variation of depth, the element mapping of the film in Fig. 2c, 2e and 2f are presented in Fig. 2g–i. The strong carbon signal belonging to multilayer graphene was weakened when the composite film was stripped off the loosest layer on the outermost surface, whereas the Ti signal belonging to $Ti_3C_2T_x$ was enhanced at the same time, inferring that there was a compositional gradient in the $Ti_3C_2T_x$/graphene composite film and the contents of graphene and $Ti_3C_2T_x$ were negatively and positively correlated with the depth in the film respectively. However, due to the random stack of multilayer graphene and $Ti_3C_2T_x$, it was of significant difficulty to quantify the compositional gradient. Therefore, for more rigor, we define this component gradient as a “quasi-component gradient”. The formation of the quasi-component gradient may be due to the fact that the $Ti_3C_2T_x$ particles with smaller size will preferentially settle to the bottom layer through the interspace between the loosely stacked multilayer graphene sheets during the vacuum filtration process. When being transformed onto a PDMS substrate to form a strain sensor, the $Ti_3C_2T_x$/graphene film was overturned, leading to the fact that the surface of the film was mainly composed of closely stacked $Ti_3C_2T_x$ particles, while the bottom layer had the higher graphene content.

4. Sensing performance analysis

The strain-sensing performance of the strain sensors based on $Ti_3C_2T_x$/graphene films was investigated. Fig. 3a demonstrates the typical relative resistance variation-strain ($\Delta R/R_0$-ε) curve of the $Ti_3C_2T_x/G_{0.5}$/PDMS based strain sensor. In general, ΔR is defined as ($R-R_0$) where R, R_0 and ε stand for the resistance under varying strain, the initial resistance under no load, and strain, respectively. The slope of $\Delta R/R_0$-ε curve, which is usually expressed in GF, was used to evaluate the sensitivity of a strain sensor. It can be seen that the $\Delta R/R_0$-ε curve of the strain sensor based on $Ti_3C_2T_x/G_{0.5}$/PDMS was divided into two stages. During the strain range of 0–52.6%, the GF was quantified as 190.8, while the GF in the strain range of 52.6%–74.1% was increased to 1148.2 with the coefficient of determination (R^2) of these two curves higher than 0.98. Fig. 4 shows the comparison of sensing performances in the first linear range of strain sensors with the total strain sensing range larger than 50%. From the Fig. we distinguished whether the sensor possessed a high GF in the small strain region and whether GF can be maintained high and steady over a wide strain range, which is considered as two critical indicators for a desired sensor. It is obvious that very limited strain sensors in current reports can maintain GFs above 100 over wide strain ranges, whereas the strain sensor based on $Ti_3C_2T_x/G_{0.5}$/PDMS achieved a high and stable GF (over 190.8) over a wide strain range (0–52.6%), and a highly linear response can also be achieved under the strain range of 52.6–74.1%, which is more desirable than the strain sensors that only demonstrated high sensitivities at large strains. To conform the reproducibility of the $Ti_3C_2T_x/G_{0.5}$/PDMS based strain sensor, the $\Delta R/R_0$-ε curves of other five samples prepared with the same experimental conditions have been prepared and tested. As seen in Fig. A8, five curves have the same trend and all have good linear

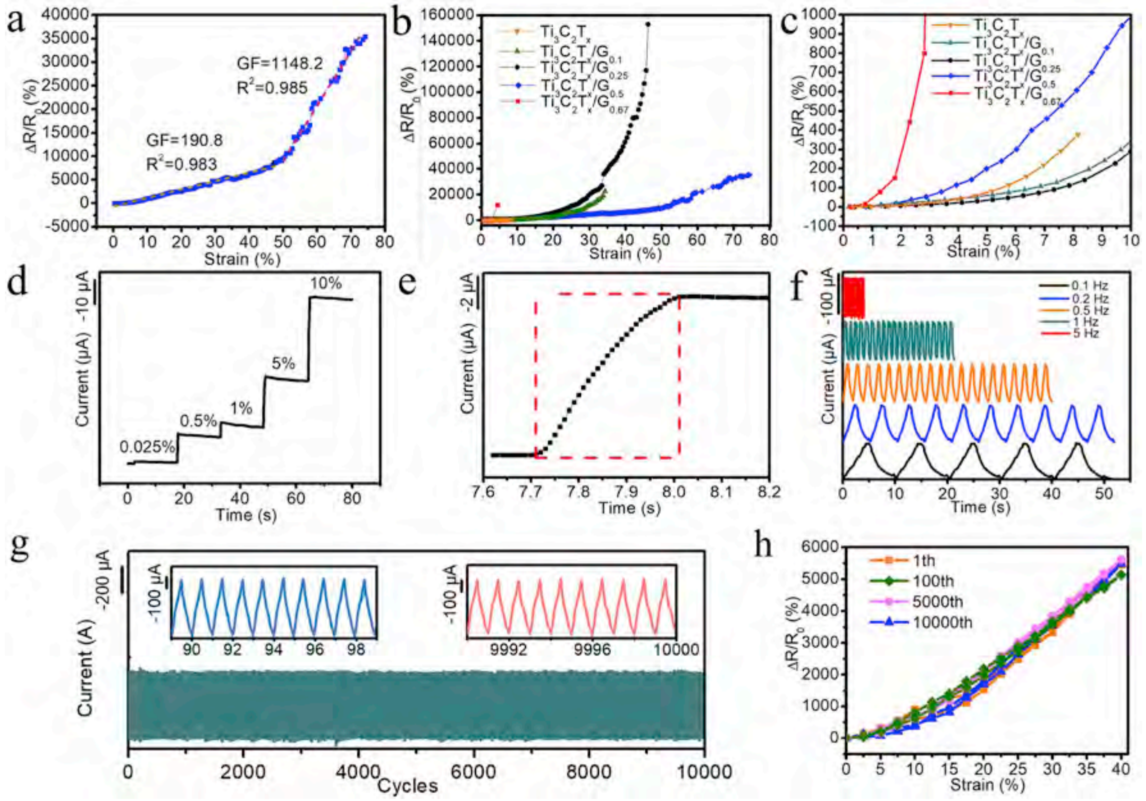

Fig. 3. Strain sensing properties of the $Ti_3C_2T_x$/graphene/PDMS based strain sensors. a) A relative resistance variation-strain curve of the $Ti_3C_2T_x/G_{0.5}$/PDMS based strain sensor at a stretching rate of 60% min^{-1}. b) Relative resistance variation-strain curves of the $Ti_3C_2T_x$/graphene/PDMS based strain sensors with various graphene contents at a stretching rate of 60% min^{-1}. c) Reproduction of the curve in b) within a 0–10% strain range. d) Current signals of the strain senor under a step-increasing strain from 0.025% to 10%. e) Real-time current-time curve under a strain of 1% at a stretching rate of 40 mm s^{-1}. f) Current changes of the strain sensor at various frequencies under a 10% strain. g) Cycling durability test under a 40% strain at a stretching rate of 60% min^{-1}. The insets are the magnified views around 100th and 10000th cycles. h) Relative resistance-strain curves of specific stretch/release cycles under a 40% strain.

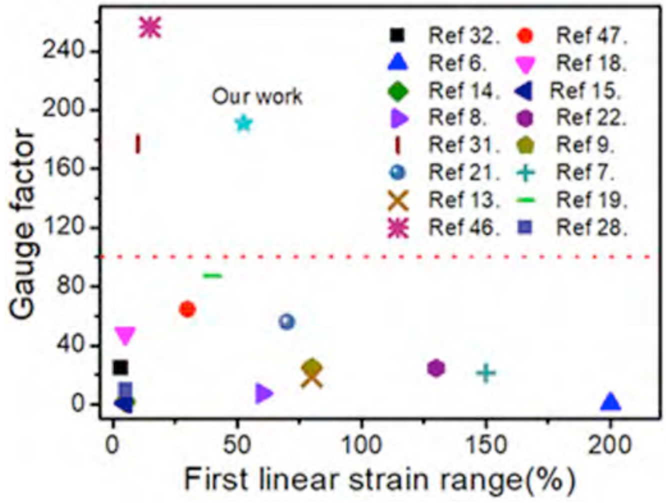

Fig. 4. Comparison of the sensing performance in the first linear-response strain range of strain sensors with the total strain sensing range larger than 50%.

response over a strain range of more than 50%.

In order to maximize the synergistic effect of $Ti_3C_2T_x$ and multilayer graphene, we investigated the effects of graphene content on the sensing performance of the $Ti_3C_2T_x$/graphene/PDMS based sensors. Through the information revealed in Fig. 3b, it is obvious that different graphene contents lead to significant differences in the sensing performances. For the pure $Ti_3C_2T_x$ based strain sensor, it exhibited a GF of 13.4 within a strain range of 4.6% and 88.1 within a range of 8.2%, producing low performances in both sensitivity and stretchability. As the content of graphene increases (≤50 wt%), the maximum working range of strain sensors gradually expanded to 34.1% (for $Ti_3C_2T_x/G_{0.1}$), 45.7% (for $Ti_3C_2T_x/G_{0.25}$) and 74.1% (for $Ti_3C_2T_x/G_{0.5}$) respectively, which was mainly attributed to the fact that graphene increased the connectivity of conducting pathways. The detail sensitivity and working range for each sample are presented in Table A1. It is obvious that the $\Delta R/R_0$-ε curve of the $Ti_3C_2T_x/G_{0.5}$/PDMS based sensor was more liner than other curves and functioned as a better choice as a strain sensor. By contrast, the working range of the $Ti_3C_2T_x/G_{0.67}$/PDMS based sensor was only 4.3%, and the relative resistance experienced a sudden increase in the range of 2.8–4.3%, which may be due to the fact that the excessive addition of multilayer graphene lead to a loose structure of the film and cannot maintain the conductive pathways. Fig. 3c reproduces the curves within the strain range of 0–10%. It is noticed that except for the $Ti_3C_2T_x/G_{0.67}$/PDMS film with low stretchability, the relative resistance of the strain sensor based on the $Ti_3C_2T_x/G_{0.5}$/PDMS film increased fastest during the small strain ranges, indicating the highest sensitivity in this range. Undoubtedly, 50 wt% was the best content of graphene when sensitivity, working range and linearity were taken into consideration.

Other strain sensing tests were conducted where the $Ti_3C_2T_x/G_{0.5}$/PDMS based strain sensors were used as testing samples. Fig. 3d shows the current signal of the strain sensor as a function of testing time under the step strain of 0.025%, 0.5%, 1%, 5% and 10%. It is observed that the current signal varied with the strain changing with a positive correlation. Besides, the detection limit of the sensor was quantified as 0.025%,

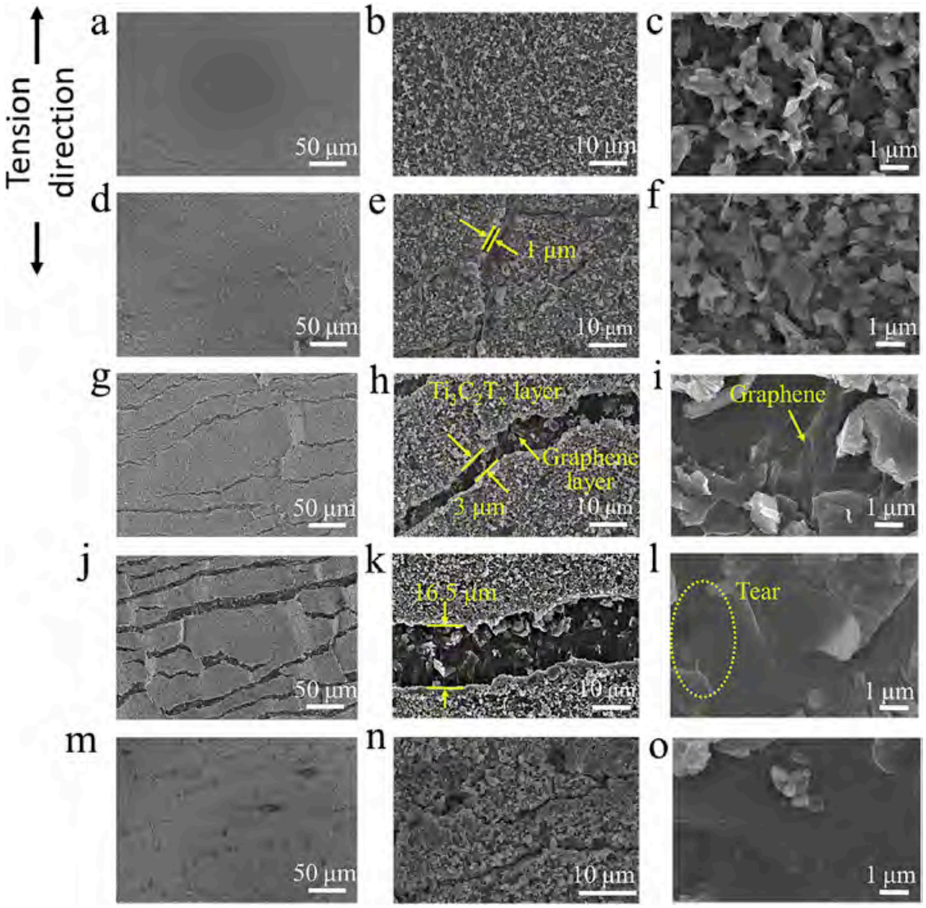

Fig. 5. Top-view SEM images of the $Ti_3C_2T_x$/graphene/PDMS based strain sensor being stretched at various strains during the initial stretching/releasing cycle: a-c) 0%, d-f) 10%, g-i) 30%, j-l) 70%, and back to m-o) 0%.

which was low enough to detect almost all subtle deformations of human bodies. The response time of the strain sensor was determined by collecting the real-time current signal under a very small strain of 1%. As is shown in Fig. 3e, the response time was quantified as 130 ms, enabling the monitoring of fast and sequential movements in real time. The current signal of the strain sensor being stretched at different frequencies was recorded in Fig. 3f. Note that the current response commendably followed the changes of the frequency at the range of 0.1–5 Hz, and the height of all current peaks was consistent under the strain of 10%, indicating that the strain sensor can satisfy the high-frequency reciprocating motion. Fig. 3g depicts the cycling durability test of the sensor under a cyclic strain of 0–40% at a stretching rate of 60% min^{-1}. Apparently, there was no obvious attenuation of current signals after the strain senor was tested for 10000 cycles, confirming high cycling stability of the sensor. The I-ε curves of the strain sensor under 90-100th, and 9990-10000th cycles are inserted in Fig. 3g, and the $\Delta R/R_0$-ε curves of specific stretch/release cycles under a 40% strain are presented in Fig. 3h, which further validate the high repeatability of the $Ti_3C_2T_x$/graphene/PDMS based strain sensor.

5. Sensing mechanism analysis

To investigate the sensing mechanism of the $Ti_3C_2T_x$/graphene/PDMS based strain sensor, the initial stretching/release cycle of the sensor was reproduced, and the difference on the morphology of the sensing material under various strain state was observed. As shown in Fig. 5a-c, before stretching, there were no obvious cracks on the composite film, while countless small $Ti_3C_2T_x$ particles and some graphene sheets were densely packed on the surface of the film. With the application of a tensile strain of 10% (Fig. 5d–f), some large cracks with a width of 1 µm approximatively perpendicular to the tensile direction appeared on the surface of the film, while the stacking density of the $Ti_3C_2T_x$ particles and graphene sheets didn't seem to change significantly, indicating that the film released tensile stress mainly by generating cracks instead of mutual movements between $Ti_3C_2T_x$ particles and graphene sheets. As the strain was further increased to 30% (Fig. 5g–i), the crack size on the film was further enlarged to more than 3 µm, and surprisingly there was another conductive layer exposed through the cracks. To investigate the composition of the bottom layer, EDS element mapping of the $Ti_3C_2T_x/G_{0.5}$/PDMS film under a stretching state was performed (see Fig. 6a-f). Remarkably, the C and Si signals were very strong for the bottom layer, which was correlated with PDMS and graphene, respectively, while the Ti signal was almost absent in this layer while concentrated in the upper layer. Considering the fact that the multilayer graphene prepared by the electrochemical method had almost no hydrophilic functional groups and they loosely packed on the surface of the film, it was reasonably speculated that when the composite film was transferred onto the PDMS substrate (note: the film is turned upside-down), the loosely stacked graphene was easily infiltrated by PDMS and a continuous conductive layer mainly consisting of multilayer graphene and PDMS was successfully formed. Since $Ti_3C_2T_x$ is hydrophilic and cannot be infiltrated by PDMS, there was almost no $Ti_3C_2T_x$ in the bottom layer. Therefore, the $Ti_3C_2T_x$/graphene/PDMS composite film had a layered structure, in which the upper layer formed by densely stacked $Ti_3C_2T_x$ and graphene was brittle and contributed to the rapid decrease in the conductance of the sensor under a relative small strain by generating cracks, rendering a steady GF of 190.8 within a wide strain range (0–52.6%). The bottom graphene/PDMS layer was

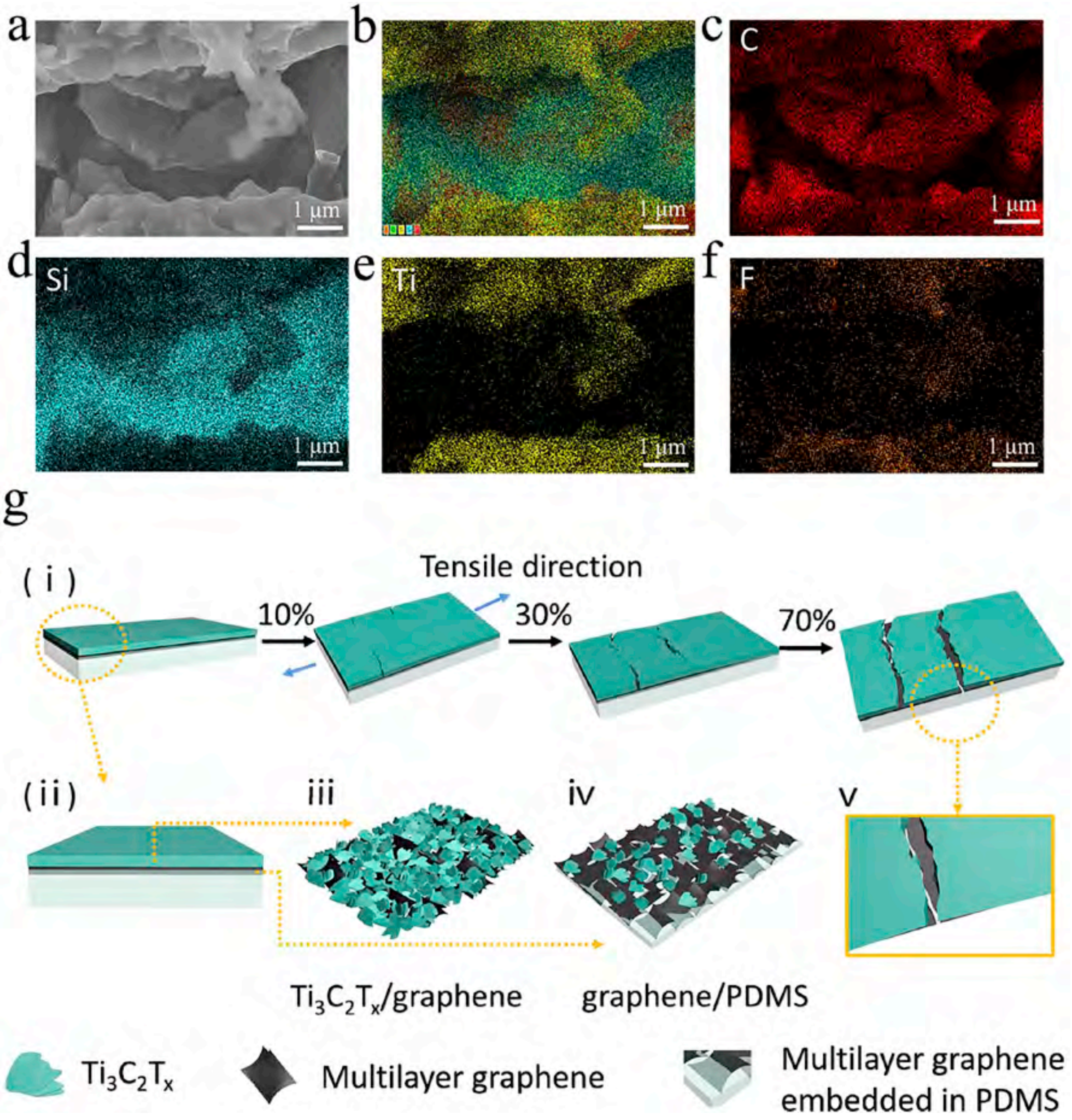

Fig. 6. a–f) EDS element mapping of the $Ti_3C_2T_x/G_{0.5}$/PDMS structure when the strain sensor is stretched to 70%. g) Schematic diagram of the $Ti_3C_2T_x/G_{0.5}$/PDMS structure based strain sensor at various stretching states.

more flexible, and served to guarantee the connectivity of conductive pathways. The lubricity of multilayer graphene may facilitate its slippage and result in a wide sensing range. It is worth noting that the upper and bottom layers of the $Ti_3C_2T_x$/graphene/PDMS layered structure were not completely discrete. Due to the existence of quasi-component gradients, there was a transition layer composed of $Ti_3C_2T_x$ and graphene to maintain the connectivity between the upper and bottom layers during the stretching process, thus ensuring the superb durability and stability of the sensor. Fig. 5j-l depict the morphology of the film when the strain sensor was stretched to 70%. The large cracks perpendicular to the tensile direction continued to expand to about 16.5 μm. Note that the graphene/PDMS layer in the cracks was torn to an extent, which explains the significant increases in the electrical resistance of the sensor under the strain range of 52.6%–74.1%, further confirming the function of the graphene/PDMS layer on maintaining conductivity within the entire stretching process. With the strain released completely (see Fig. 5m–o), both large cracks in the upper layer and crevices in the graphene/PDMS layer coalesced, guaranteeing the cycling duration of the strain sensor.

Fig. 6g schematically demonstrates the sensing mechanism of the $Ti_3C_2T_x$/graphene/PDMS layered structure based strain sensor. The response of the whole stretching process was briefly divided into two stages. During the first stage (the first linear response range), cracks generated and uniformly propagated in the upper layer to dissipate the tensile stress while the bottom layer exhibited negligible changes, rendering a highly sensitive and linear response of the sensor. During the second stage (the second linear response range), cracks in the upper layer further widened, accompanied by the slippage of graphene sheets and local avulsion of the bottom layer, generating a much higher GF in this stage. All in all, the balance between the destruction and maintaining of the conductive pathways through the synergetic motion of the upper and bottom layers ensured the high and steady GFs of the senor in a wide strain range.

For comparison, the sensing mechanisms of the pure $Ti_3C_2T_x$ and $Ti_3C_2T_x/G_{0.67}$/PDMS based strain sensors were investigated as well. As shown in Fig. A6, the variations on the microstructures of the pure $Ti_3C_2T_x$ strain sensor with strain were almost the same as that of the upper layer of the $Ti_3C_2T_x$/graphene/PDMS layered structure based

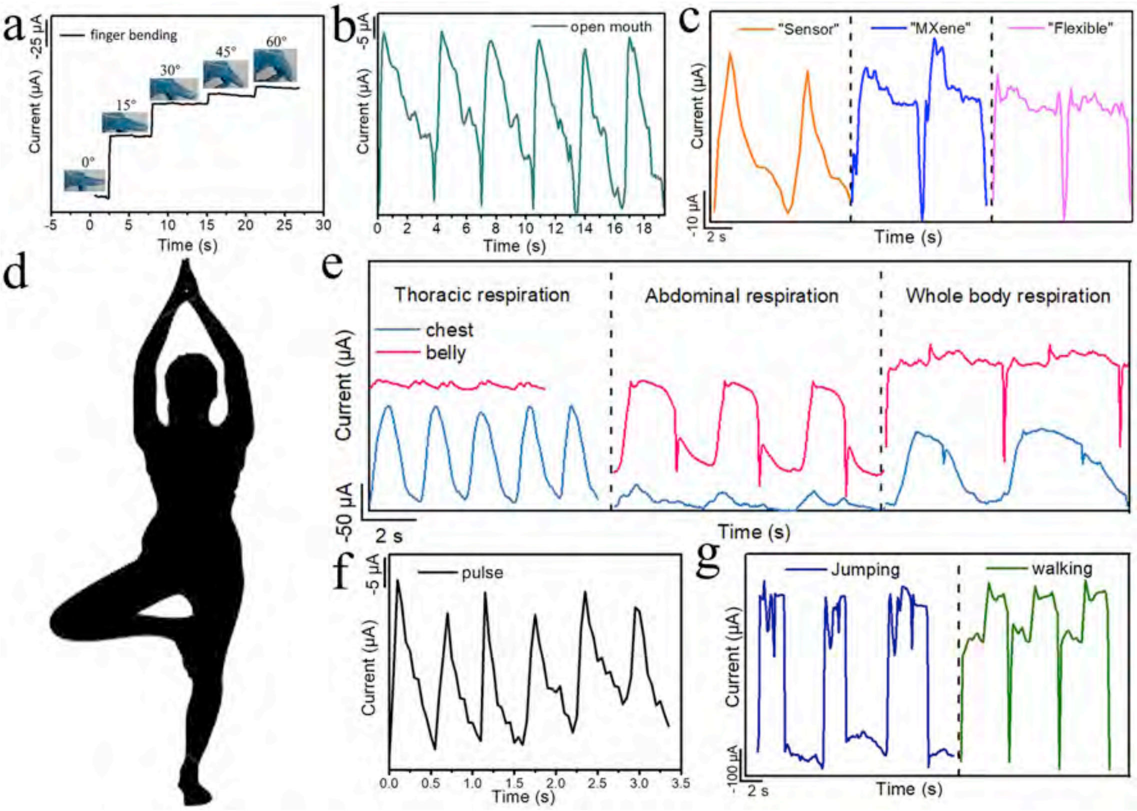

Fig. 7. The current signals of the $Ti_3C_2T_x$/Graphene strain sensors in monitoring a) finger bending. Inset: digital photographs of a finger bent to the corresponding positions; b) mouth opening and c) phonation. d) The schematic diagram of mannequin with recorded current signals in e) breathing modes in yoga; f) pulse; and g) slow walking and jumping.

sensor, except that the pure $Ti_3C_2T_x$ film is not infiltrated by PDMS because of the incompatibility between these two. The non-conductive flexible PDMS substrate was exposed after the fracture of the $Ti_3C_2T_x$ film (Fig. A6f), which was responsible for the interdiction of conductive pathways and the narrow sensing range of the sensor. By contrast, due to the excessive content of the multilayer graphene, the $Ti_3C_2T_x/G_{0.67}$/PDMS film was too brittle and susceptible to cracking and shedding when the sensor was stretched, resulting in a rapid increase in the resistance of the sensor within a small strain range (Fig. A7).

6. Human activities detection

In view of the excellent sensing performances of the $Ti_3C_2T_x$/graphene/PDMS based strain sensor, we attached the sensor to different parts of human bodies for the full-range detection of human activities. For the capture of vigorous physiological signals, the strain sensor was attached to the knuckle area to record the changes in current signals during the bending of a finger from 0° to 90° (Fig. 7a) and was attached to the cheek area to monitor the process of opening-closing movements of a mouth (Fig. 7b). In sensing more substantial movements, we mounted the strain sensor on a knee joint, and the joint-related movements such as slow walking and jumping (Fig. 7g) were easily discriminated due to the regular and differentiated repetitive pattern of the response curves. To monitor subtle signals such as phonation and pulses, the strain sensor was attached to the throat and the wrist areas, respectively. Fig. 7c demonstrates the responsive curves with significant characteristics and repeatabilities, in response to speaking different words such as "sensor", "MXene" and "flexible", indicating the effective applications in phonation recognitions. In Fig. 7f, the response curve clearly disclosed the characteristic peaks of human pulses including percussion, tidal and diastolic peaks. In order to further confirm the high sensitivity of the sensor, we attached sensors to the abdomen and chest of human bodies to distinguish three breathing patterns in yoga. The changes in current signals of the two sensors during abdominal breathing, chest breathing and whole body breathing were recorded (Fig. 7e). The current curves had obvious differences in intensities and peaking shapes, which can be used for recognizing breathing patterns. In a word, the capabilities on monitoring subtle and substantial movements equip the $Ti_3C_2T_x$/graphene/PDMS based strain sensor with great application potentials in monitoring human physiological and robotic signals.

7. Conclusion

In summary, a $Ti_3C_2T_x$/graphene/PDMS composite film with layered structure was presented. The $Ti_3C_2T_x$ dominated upper layer was brittle and tended to generate cracks to dissipate stresses when being stretched, while the graphene/PDMS bottom layer kept contact to maintain the conductive pathways. The synergetic motion of the upper and bottom layers rendered the film with highly sensitive and linear responses to strains in a wide strain range. Sensors based on the $Ti_3C_2T_x$/graphene/PDMS film exhibited both a high GF and a wide sensing range (a GF of 190.8 in the strain range of 0–52.6% and 1148.2 within the range of 52.6–74.1%), as well as a low limit of detection (~0.025%) and superb cycling stabilities (over 5000 cycles under the strain of 40%). Full-range human motion detection was conducted to demonstrate the practicability of the sensor. This work may shed new lights on enhancing the comprehensive performances of strain sensors from the view of composition design.

Acknowledgements

The work was financially supported by National Natural Science Foundation of China (Grant No.61871368), Youth Innovation

Promotion Association CAS Shanghai Science, Technology Rising Star Project (17QA1404700), and Young Elite Scientists Sponsorship Program by CAST. The work was supported by the State Key Laboratory of Robotics.

Appendix A. Supplementary data

Supplementary data to this article can be found online at https://doi.org/10.1016/j.nanoen.2019.104134.

References

[1] M. Amjadi, K.-U. Kyung, I. Park, M. Sitti, Stretchable, skin-mountable, and wearable strain sensors and their potential applications: a review, Adv. Funct. Mater. 26 (2016) 1678–1698. https://doi.org/10.1002/adfm.201504755.

[2] T. Yang, D. Xie, Z. Li, H. Zhu, Recent advances in wearable tactile sensors: materials, sensing mechanisms, and device performance, Mater. Sci. Eng., R. 115 (2017) 1–37. https://doi.org/10.1016/j.mser.2017.02.001.

[3] H. Zhang, W. Niu, S. Zhang, Extremely stretchable, stable, and durable strain sensors based on double-network organogels, ACS Appl. Mater. Interfaces 10 (2018) 32640–32648. https://doi.org/10.1021/acsami.8b08873.

[4] T.Q. Trung, N.E. Lee, Flexible and stretchable physical sensor integrated platforms for wearable human-activity monitoringand personal healthcare, Adv. Mater. 28 (2016) 4338–4372. https://doi.org/10.1002/adma.201504244.

[5] A.P. Morteza Amjadi, Sangjun Lee, Seunghwa Ryu, Inkyu Park, Highly stretchable and sensitive strain sensor based on silver nanowire elastomer nanocomposite, ACS Nano 8 (2014) 5154–5163. https://doi.org/10.1021/acs.nanolett.5b01505.

[6] R. Wang, N. Jiang, J. Su, Q. Yin, Y. Zhang, Z. Liu, H. Lin, F.A. Moura, N. Yuan, S. Roth, R.S. Rome, R. Ovalle-Robles, K. Inoue, S. Yin, S. Fang, W. Wang, J. Ding, L. Shi, R.H. Baughman, Z. Liu, A Bi-sheath fiber sensor for giant tensile and torsional displacements, Adv. Funct. Mater. 27 (2017) 1702134. https://doi.org/10.1002/adfm.201702134.

[7] L. Li, H. Xiang, Y. Xiong, H. Zhao, Y. Bai, S. Wang, F. Sun, M. Hao, L. Liu, T. Li, Z. Peng, J. Xu, T. Zhang, Ultrastretchable fiber sensor with high sensitivity in whole workable range for wearable electronics and implantable medicine, Adv. Sci. (Weinheim, Ger.). 5 (2018) 1800558. https://doi.org/10.1002/advs.201800558.

[8] S. Park, S. Ahn, J. Sun, D. Bhatia, D. Choi, K.S. Yang, J. Bae, J.-J. Park, Highly bendable and rotational textile structure with prestrained conductive sewing pattern for human joint monitoring, Adv. Funct. Mater. 29 (2019) 1808369. https://doi.org/10.1002/adfm.201808369.

[9] M. Zhang, C. Wang, H. Wang, M. Jian, X. Hao, Y. Zhang, Carbonized cotton fabric for high-performance wearable strain sensors, Adv. Funct. Mater. 27 (2017) 1604795. https://doi.org/10.1002/adfm.201604795.

[10] Y. Xin, J. Zhou, R. Tao, X. Xu, G. Lubineau, Making a bilateral compression/tension sensor by pre-stretching open-crack networks in carbon nanotube papers, ACS Appl. Mater. Interfaces 10 (2018) 33507–33515. https://doi.org/10.1021/acsami.8b08166.

[11] Z. Cao, R. Wang, T. He, F. Xu, J. Sun, Interface-controlled conductive fibers for wearable strain sensors and stretchable conducting wires, ACS Appl. Mater. Interfaces 10 (2018) 14087–14096. https://doi.org/10.1021/acsami.7b19699.

[12] J.T. Muth, D.M. Vogt, R.L. Truby, Y. Menguc, D.B. Kolesky, R.J. Wood, J.A. Lewis, Embedded 3D printing of strain sensors within highly stretchable elastomers, Adv. Mater. 26 (2014) 6307–6312. https://doi.org/10.1002/adma.201400334.

[13] J. Ma, P. Wang, H. Chen, S. Bao, W. Chen, H. Lu, Highly sensitive and large-range strain sensor with a self-compensated two-order structure for human motion detection, ACS Appl. Mater. Interfaces 11 (2019) 8527–8536. https://doi.org/10.1021/acsami.8b20902.

[14] Y. Cai, J. Shen, Z. Dai, X. Zang, Q. Dong, G. Guan, L.J. Li, W. Huang, X. Dong, Extraordinarily stretchable all-carbon collaborative nanoarchitectures for epidermal sensors, Adv. Mater. 29 (2017) 1606411. https://doi.org/10.1002/adma.201606411.

[15] Y. Wang, Y. Wang, Y. Yang, Graphene-Polymer nanocomposite-based redox-induced electricity for flexible self-powered strain sensors, Adv. Energy Mater. 8 (2018) 1800961. https://doi.org/10.1002/aenm.201800961.

[16] S. Conor, U.K. Boland, Claudia Backes, Arlene O'Neill, Joe McCauley, Duane Shane, Ravi Shanker, Yang Liu, Izabela Jurewicz, Alan B. Dalton, Jonathan N. Coleman, Sensitive, high-strain, high-rate bodily motion sensors based on graphene rubber composites, ACS Nano 8 (2014) 8819–8830. https://doi.org/10.1021/nn503454h.

[17] S. Wu, S. Peng, Z.J. Han, H. Zhu, C.H. Wang, Ultrasensitive and stretchable strain sensors based on mazelike vertical graphene network, ACS Appl. Mater. Interfaces 10 (2018) 36312–36322. https://doi.org/10.1021/acsami.8b15848.

[18] J. Zhou, X. Xu, Y. Xin, G. Lubineau, Coaxial thermoplastic elastomer-wrapped carbon nanotube fibers for deformable and wearable strain sensors, Adv. Funct. Mater. 28 (2018) 1705591. https://doi.org/10.1002/adfm.201705591.

[19] S. Wang, P. Xiao, Y. Liang, J. Zhang, Y. Huang, S. Wu, S.-W. Kuo, T. Chen, Network cracks-based wearable strain sensors for subtle and large strain detection of human motions, J. Mater. Chem. C. 6 (2018) 5140–5147. https://pubs.rsc.org/10.1039/c8tc00433a.

[20] J. Lee, S. Pyo, D.S. Kwon, E. Jo, W. Kim, J. Kim, Ultrasensitive strain sensor based on separation of overlapped carbon nanotubes, Small (2019) 1805120. https://doi.org/10.1002/smll.201805120.

[21] J. Oh, J.C. Yang, J.O. Kim, H. Park, S.Y. Kwon, S. Lee, J.Y. Sim, H.W. Oh, J. Kim, S. Park, Pressure insensitive strain sensor with facile solution-based process for tactile sensing applications, ACS Nano 12 (2018) 7546–7553. https://doi.org/10.1021/acsnano.8b03488.

[22] K.H. Kim, N.S. Jang, S.H. Ha, J.H. Cho, J.M. Kim, Highly sensitive and stretchable resistive strain sensors based on microstructured metal nanowire/elastomer composite films, Small 14 (2018) 1704232. https://doi.org/10.1002/smll.201704232.

[23] R. Nur, N. Matsuhisa, Z. Jiang, M.O.G. Nayeem, T. Yokota, T. Someya, A highly sensitive capacitive-type strain sensor using wrinkled ultrathin gold films, Nano Lett. 18 (2018) 5610–5617. https://doi.org/10.1021/acs.nanolett.8b02088.

[24] J. Kim, S.W. Lee, M.H. Kim, O.O. Park, Zigzag-shaped silver nanoplates: synthesis via ostwald ripening and their application in highly sensitive strain sensors, ACS Appl. Mater. Interfaces 10 (2018) 39134–39143. https://doi.org/10.1021/acsami.8b11322.

[25] K.K. Kim, S. Hong, H.M. Cho, J. Lee, Y.D. Suh, J. Ham, S.H. Ko, Highly sensitive and stretchable multidimensional strain sensor with prestrained anisotropic metal nanowire percolation networks, Nano Lett. 15 (2015) 5240–5247. https://doi.org/10.1021/acs.nanolett.5b01505.

[26] C.S. Boland, U. Khan, H. Benameur, J.N. Coleman, Surface coatings of silver nanowires lead to effective, high conductivity, high-strain, ultrathin sensors, Nanoscale 9 (2017) 18507–18515. https://pubs.rsc.org/10.1039/c7nr06685f.

[27] J. Lee, S. Kim, J. Lee, D. Yang, B.C. Park, S. Ryu, I. Park, A stretchable strain sensor based on a metal nanoparticle thin film for human motion detection, Nanoscale 6 (2014) 11932–11939. https://pubs.rsc.org/10.1039/c4nr03295k.

[28] S. Gong, D. Lai, B. Su, K. Si, Z. Ma, L. Yap, P. Guo, W. Cheng, Highly stretchy black gold E-skin nanopatches as highly sensitive wearable biomedical sensors, Adv. Electron. Mater. (2015) 1400063. https://doi.org/10.1002/aelm.201400063.

[29] Y. Wang, S. Gong, S. Wang, X. Yang, Y. Ling, L. Yap, D. Dong, G. Simon, W. Cheng, Standing enokitake-like nanowire films for highly stretchable elastronics, ACS Nano 12 (2018) 9742–9749. https://doi.org/10.1021/acsnano.8b05019.

[30] X. Li, R. Zhang, W. Yu, K. Wang, J. Wei, D. Wu, A. Cao, Z. Li, Y. Cheng, Q. Zheng, R. S. Ruoff, H. Zhu, Stretchable and highly sensitive graphene-on-polymer strain sensors, Sci. Rep. 2 (2012) 870. https://doi.org/10.1038/srep00870.

[31] J. Ryu, J. Kim, J. Oh, S. Lim, J.Y. Sim, J.S. Jeon, K. No, S. Park, S. Hong, Intrinsically stretchable multi-functional fiber with energy harvesting and strain sensing capability, Nano Energy 55 (2019) 348–353. https://doi.org/10.1016/j.nanoen.2018.10.071.

[32] X. Shi, S. Liu, Y. Sun, J. Liang, Y. Chen, Lowering internal friction of 0D-1D-2D ternary nanocomposite-based strain sensor by fullerene to boost the sensing performance, Adv. Funct. Mater. 28 (2018) 1800850. https://doi.org/10.1002/adfm.201800850.

[33] M. Naguib, M. Kurtoglu, V. Presser, J. Lu, J. Niu, M. Heon, L. Hultman, Y. Gogotsi, M.W. Barsoum, Two-dimensional nanocrystals produced by exfoliation of Ti_3AlC_2, Adv. Mater. 23 (2011) 4248–4253. https://doi.org/10.1002/adma.201102306.

[34] M. Naguib, V.N. Mochalin, M.W. Barsoum, Y. Gogotsi, 25th anniversary article: MXenes: a new family of two-dimensional materials, Adv. Mater. 26 (2014) 992–1005. https://doi.org/10.1002/adma.201304138.

[35] O.M. Michael Naguib, Joshua Carle, Volker Presser, Jun Lu, Lars Hultman, Yury Gogotsi, Michel W. Barsoum, Two-dimensional transition metal carbides, ACS Nano 6 (2012) 1322–1331. https://doi.org/10.1021/nn204153h.

[36] J. Zhang, H. Cao, H. Wang, Mater. Research progress of novel two-dimensional material MXene, J. Inorg. 32 (2017) 561–570. http://www.jim.org.cn/CN/10.15541/jim20160479.

[37] F. Wu, Y. Jiang, Z. Ye, Y. Huang, Z. Wang, S. Li, Y. Mei, M. Xie, L. Li, R. Chen, A 3D flower-like VO_2/MXene hybrid architecture with superior anode performance for sodium ion batteries, J. Mater. Chem. A. 7 (2019) 1315–1322. https://pubs.rsc.org/10.1039/c8ta11419f.

[38] Y.-Y. Peng, B. Akuzum, N. Kurra, M.-Q. Zhao, M. Alhabeb, B. Anasori, E.C. Kumbur, H.N. Alshareef, M.-D. Ger, Y. Gogotsi, All-MXene (2D titanium carbide) solid-state microsupercapacitors for on-chip energy storage, Energy Environ. Sci. 9 (2016) 2847–2854. https://pubs.rsc.org/10.1039/c6ee01717g.

[39] B. Anasori, M.R. Lukatskaya, Y. Gogotsi, 2D metal carbides and nitrides (MXenes) for energy storage, Nat. Rev. Mater. 2 (2017) 16098. https://doi.org/10.1038/natrevmats.2016.98.

[40] J. Luo, C. Wang, H. Wang, X. Hu, E. Matios, X. Lu, W. Zhang, X. Tao, W. Li, Pillared MXene with ultralarge interlayer spacing as a stable matrix for high performance sodium metal anodes, Adv. Funct. Mater. 29 (2019) 1805946. https://doi.org/10.1002/adfm.201805946.

[41] Z. Xiao, Z. Yang, Z. Li, P. Li, R. Wang, Synchronous gains of areal and volumetric capacities in lithium-sulfur batteries promised by flower-like porous $Ti_3C_2T_x$ matrix, ACS Nano 13 (2019) 3404–3412. https://doi.org/10.1021/acsnano.8b09296.

[42] M.A. Faisal Shahzad, Christine B. Hatter, Babak Anasori, Soon Man Hong, Chong Min Koo, Yury Gogotsi, Electromagnetic interference shielding with 2D transition metal carbides (MXenes), Science 353 (2016). http://science.sciencemag.org/content/353/6304/1137.

[43] J. Liu, H.B. Zhang, R. Sun, Y. Liu, Z. Liu, A. Zhou, Z.Z. Yu, Hydrophobic, flexible, and lightweight MXene foams for high-performance electromagnetic-interference shielding, Adv. Mater. 29 (2017) 1702367. https://doi.org/10.1002/adma.201702367.

[44] L. Xiu, Z. Wang, M. Yu, X. Wu, J. Qiu, Aggregation-resistant 3D MXene-based architecture as efficient bifunctional electrocatalyst for overall water splitting, ACS Nano 12 (2018) 8017–8028. https://doi.org/10.1021/acsnano.8b02849.

[45] I. Persson, J. Halim, H. Lind, T.W. Hansen, J.B. Wagner, L.A. Naslund, V. Darakchieva, J. Palisaitis, J. Rosen, P.O.A. Persson, 2D transition metal carbides

(MXenes) for carbon capture, Adv. Mater. 31 (2019) 1805472. https://doi.org/10.1002/adma.201805472.

[46] X. Shi, H. Wang, X. Xie, Q. Xue, J. Zhang, S. Kang, C. Wang, J. Liang, Y. Chen, Bioinspired ultrasensitive and stretchable MXene-based strain sensor via nacre-mimetic microscale "Brick-and-Mortar" architecture, ACS Nano 13 (2019) 649–659. https://doi.org/10.1021/acsnano.8b07805.

[47] Y. Cai, J. Shen, G. Ge, Y. Zhang, W. Jin, W. Huang, J. Shao, J. Yang, X. Dong, Stretchable Ti3C2Tx MXene/carbon nanotube composite based strain sensor with ultrahigh sensitivity and tunable sensing range, ACS Nano 12 (2018) 56–62. https://doi.org/10.1021/acsnano.7b06251.

[48] Y. Yang, L. Shi, Z. Cao, R. Wang, J. Sun, Strain sensors with a high sensitivity and a wide sensing range based on a Ti3C2Tx (MXene) nanoparticle-nanosheet hybrid network, Adv. Funct. Mater. (2019) 1807882. https://doi.org/10.1002/adfm.201807882.

[49] Y. Yue, N. Liu, W. Liu, M. Li, Y. Ma, C. Luo, S. Wang, J. Rao, X. Hu, J. Su, Z. Zhang, Q. Huang, Y. Gao, 3D hybrid porous Mxene-sponge network and its application in piezoresistive sensor, Nano Energy 50 (2018) 79–87. https://doi.org/10.1016/j.nanoen.2018.05.020.

[50] Y. Ma, Y. Yue, H. Zhang, F. Cheng, W. Zhao, J. Rao, S. Luo, J. Wang, Z. Jiang, Z. Liu, N. Liu, Y. Gao, 3D synergistical MXene/reduced graphene oxide aerogel for a piezoresistive sensor, ACS Nano 12 (2018) 3209–3216. https://doi.org/10.1021/acsnano.7b06909.

[51] Y. Ma, N. Liu, L. Li, X. Hu, Z. Zou, J. Wang, S. Luo, Y. Gao, A highly flexible and sensitive piezoresistive sensor based on MXene with greatly changed interlayer distances, Nat. Commun. 8 (2017) 1207. https://doi.org/10.1038/s41467-017-01136-9.

[52] H.S. Wang, S.Y. Tian, S.W. Yang, G. Wang, X.F. You, L.X. Xu, Q.T. Li, P. He, G. Q. Ding, Z. Liu, X.M. Xie, Anode coverage for enhanced electrochemical oxidation: a green and efficient strategy towards water-dispersible graphene, Green Chem. 20 (2018) 1306–1315. https://pubs.rsc.org/10.1039/c7gc03345a.

Yang Yina, received her B.S. degree in Tianjin University in 2015 is now a Ph.D. candidate in SICCAS in Prof. Sun jing's group. Her research interests are MXenes based flexible electronics.

Cao Zherui received his B.S. degree from Liaoning University in 2014 and is now a Ph.D. candidate in SICCAS in Prof. Sun jing's group. His research interests include elastic conducting fibers for electronic textiles.

He Peng received his B.S. degree (2013) from Shanghai Institute of Ceramics, Chinese Academy of Sciences (SICCAS) and PhD degree (2019) from Shanghai Institute of Microsystem and Information Technology, Chinese Academy of Sciences (SIMIT). He is currently working as an assistant researcher in SIMIT. His research work focuses on controllable preparation and application of graphene related materials including high-quality graphene, graphene oxide, water-dispersible graphene and graphene quantum dots.

Shi Liangjing received his B.S. degree from Shanghai Jiaotong University and PhD degree (2013) from SICCAS. He is now working as an assistant researcher in SICCAS. His research interests include preparation and application of CVD graphene and controllable synthesis and industrialization of metal nanowires and their applications.

Ding Guqiao received his B.S. degree and M.S. degree from Suzhou University (2001 and 2004 respectively), and received his Ph.D. from Shanghai Jiaotong University in 2007. He was engaged in material research and development at Dow Chemical in 2007.3–2009.5, and he was engaged in graphene research at Changzhou University from 2009.6 to 2010.8. Then he joined Shanghai Institute of Microsystems, Chinese Academy of Sciences in 2010.9 to engage in the research and application development of graphene materials.

Wang Ranran received her B.S. degree (2007) from China University of Petroleum and PhD degree (2012) from SICCAS. She is now working as an associate researcher in SICCAS. Her research interests include controllable synthesis and industrialization of metal nanowires, application of metal nanowires based transparent conductive films, stretchable and wearable electronics.

Sun Jing received her M.S. from Changchun Institute of Applied Chemistry and Ph.D. degree from Shanghai Institute of Ceramics in 1994 and 1997, respectively. Then she joined Shanghai Institute of Ceramics (SICCAS). She spent one year as visiting scientist in Institute for Surface Chemistry in Stockholm (YKI) between 1999 and 2000 and as a JSPS fellow in National Institute of Advanced Science and Technology (AIST) in Japan during 2002–2004. She has been appointed as a Professor in SICCAS since 2005 and now is leading a research group focusing on photo-catalysis for indoors & outdoors air-cleaning and flexible electronics.